Article:
Kelly, RW, Dorrell, RM, Burns, AD orcid.org/0000-0002-3448-7510 et al. (1 more author) (2019) The Structure and Entrainment Characteristics of Partially Confined Gravity Currents. Journal of Geophysical Research: Oceans, 124 (3). pp. 2110-2125. ISSN 2169-9291

https://doi.org/10.1029/2018JC014042

The structure and entrainment characteristics of partially-confined gravity currents

R. W. Kelly[1], R. M. Dorrell[2], A. D. Burns[3], and W. D. McCaffrey[4]

[1]EPSRC Centre for Doctoral Training in Fluid Dynamics, University of Leeds

[2]Energy and Environment Institute, University of Hull

[3]School of Chemical and Process Engineering, University of Leeds

[4]School of Earth and Environment, University of Leeds

Corresponding author: Robert Kelly (scrk@leeds.ac.uk)

Key Points:

- In partially-confined settings, channel depth is a key control on the height of a gravity current's velocity maximum.
- Both streamwise and overbank discharge rates can rapidly adjust downstream, with evidence of flow tuning and equilibration.
- The entrainment coefficient of a partially-confined flow is similar to that of a fully-confined flow with the same Richardson number.

Abstract:

Seafloor channels are the main conduit for turbidity currents transporting sediment to the deep ocean and they can extend for thousands of kilometres along the ocean floor. Although it is common for channel-traversing turbidity currents to spill onto levees and other out-of-channel areas, the associated flow development and channel-current interaction remain poorly understood; much of our knowledge of turbidity current dynamics comes from studies of fully-confined scenarios. Here we investigate the role that partial lateral confinement may play in affecting turbidity current dynamics. We report on laboratory experiments of partially-confined, dilute saline flows of variable flux rate traversing fixed, straight channels with cross-sectional profiles representative of morphologies found in the field. Complementary numerical experiments, validated against high-resolution laboratory velocity data, extend the scope of the analysis. The experiments show that partial confinement exerts a first order control on flow structure. Overbank and downstream discharges rapidly adjust over short length-scales, providing a mechanism via which currents of varying sizes can be tuned by a channel and conform to a given channel geometry. Across a wide range of flow magnitudes and states of flow equilibration to the channel, a high-velocity core remains confined within the channel with a constant ratio of velocity maximum height to channel depth. Ongoing overbank flow prevents any flow thickening due to ambient entrainment, allowing stable downstream flow evolution. Despite dynamical differences, the entrainment rates of partially-confined and fully-confined flows remain comparable for a given Richardson number.

1 Introduction:

Seafloor channels are the main conduits through which turbidity currents transport sediment from the continental shelf to the deep ocean [Meiburg and Kneller, 2010; Peakall and Sumner, 2015]. The submarine fans that they form are some of the largest sedimentary accumulations on Earth [Curray et al., 2002; Talling et al., 2007]. Due to the inherent challenges the deep-water environment poses, only recently have direct field measurements become more widespread [Khripounoff et al., 2003; Xu, 2010; Sumner et al., 2013; 2014; Talling et al., 2013; Dorrell et al., 2014; 2016; Azpiroz-Zabala et al., 2017]. In comparison there has been a long history of model development based on laboratory experiments [e.g. Ellison and Turner, 1957; Middleton, 1966; Garcia and Parker, 1983; Bonnecaze et al., 1993; Buckee et al., 2001; Keevil et al., 2006; Straub et al., 2008; Islam and Imran, 2010; Sequeiros et al., 2010] and numerical simulations [e.g. Eidsvik and Brørs, 1989; Imran et al., 2004; Huang et al., 2005; Cantero et al., 2009; Abd El-Gawad et al., 2011; Giorgio Serchi et al., 2011; Dorrell et al., 2014; Kneller et al., 2016].

The majority of these studies were conducted within fully-confined channels. Yet the partially-confined channel-

levee component of natural systems usually extends much further than the fully-confined canyons that feed them [Normark and Damuth, 1997; Klaucke et al., 1998; Meiburg and Kneller, 2010; Nakajima and Kneller, 2013]. Those studies that do consider unconfined/partially-confined settings have been run over erodible beds [Mohrig and Buttles, 2007; Straub et al., 2008; De Leeuw et al., 2016] and tend to focus on morphological evolution and channel inception rather than flow dynamics. While such studies increase knowledge of channel and system development, the evolving channel geometries limit the consistency of flow data measured from successive currents.

The dynamics and behaviour of partially-confined flows, where the current can overspill onto the levees, are arguably far more complex and difficult to predict than for fully confined flows. Differing levels of confinement lead to changes in the ratios of ambient entrainment and overbank losses, but a systematic review of the flow field under a range of confinements is lacking. Mohrig and Buttles [2007] defined channelised, quasi-channelised and unconfined regimes based on the advancement of the flow front, but without presentation of detailed flow velocity or density data.

To date, it is fully-confined studies that have been widely used to explain and predict the structure and properties of gravity currents. Parker et al. [1987] conducted straight channel experiments and reviewed previous experimental data to find a Richardson number dependent expression for the entrainment coefficient of a flow,

$$e_W = \frac{0.075}{\sqrt{1 + 718Ri^{2.4}}}. \quad (1)$$

The rate at which a flow entrains ambient fluid is a key factor in both its spatial and temporal development and could help to provide an explanation as to why turbidity currents can travel for thousands of km [Meiburg and Kneller, 2010]. Kneller et al. [2016] used numerical simulations to show that, under certain conditions, turbidity currents can have a stably stratified upper shear layer (Figure 1) with little mixing and low velocity gradients, resulting in a reduction in ambient entrainment; when predicting flow characteristics the use of bulk variables to approximate local variables was also questioned (such as using the bulk Richardson number as a proxy for the gradient Richardson number, a measure of stratification stability). In another fully-confined experiment, Sequeiros et al. [2010] observed a dependence of the velocity structure of the flow on the Richardson number, attributed to changes in stratification stability. The velocity profiles of subcritical flows (Ri>1) exhibited a velocity maximum close to the top of the flow, although a large bed roughness is likely to have caused this. This is in contrast to previously observed profiles where the outer shear layer is 5-10 times thicker than the inner layer

[Meiburg and Kneller, 2010]. Additionally, Sequeiros [2012] suggested that channel morphology can be used to predict Richardson or Froude numbers and subsequently flow conditions. However, this approach has limitations for erosional or bypassing flows as it does not take into account Reynolds-dependent turbulent effects in the lower boundary [Imran et al., 2016]. Also, high velocity maximum heights were not replicated in the simulations of Kneller et al. [2016], despite the stably stratified layer, nor in further experiments of subcritical flows which found limited dependence on Richardson number [Stagnaro and Pittaluga, 2014].

Regardless of the debate over confined-flow structure, the kinematics of a partially-confined flow must be fundamentally different due to the occurrence of overspill. Here, saline flow experiments have been conducted in a straight fixed channel with a channel-levee profile designed to be a realistic representation of morphology found in the field. Velocity data for a range of flow magnitudes has been captured (Table 2) with the aim of analysing partially-confined flow dynamics, entrainment characteristics and flow evolution.

Additionally, numerical simulations using a RANS (Reynolds-averaged Navier-Stokes) model have been used both to extend the range of flow conditions that are possible in the laboratory and to produce data for the whole flow field.

Variable	Expression
Flow depth	$h = \frac{\left(\int_0^\infty \lvert u\rvert \, dz\right)^2}{\int_0^\infty \lvert u\rvert^2 \, dz}$, where $\lvert u\rvert = \sqrt{u^2 + v^2}$
Depth-averaged velocity	$U = \frac{\int_0^\infty u \, dz}{h}, V = \frac{\int_0^\infty v \, dz}{h}, \lvert U\rvert = \frac{\int_0^\infty \lvert u\rvert \, dz}{h}$
Reynolds number	$Re = \frac{\lvert U\rvert h}{\nu}$
Froude number	$Fr = \frac{\lvert U\rvert}{\sqrt{g'h}}$
Richardson number	$Ri = \frac{g'h}{\lvert U\rvert^2}$

Reduced gravity	$g' = g\frac{\bar{\rho} - \rho_{ambient}}{\rho_{ambient}}$, where $\bar{\rho} = \frac{\int_0^\infty \rho \, dz}{h}$
Gradient Richardson number	$Ri_g = \frac{-g\frac{\partial \rho}{\partial z}}{\rho\left(\frac{\partial \lvert u \rvert}{\partial z}\right)^2}$

Table 1: Variable and notation definitions

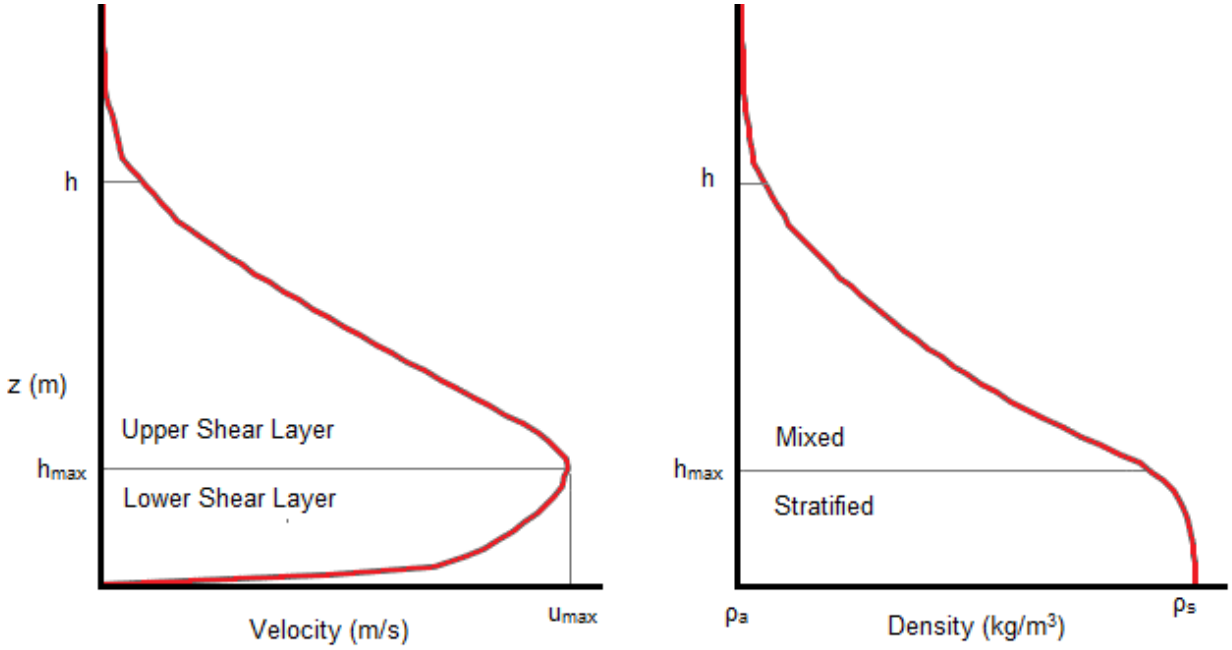

Figure 1: Velocity and density profiles for a gravity current generated by the release of a saline solution into an ambient fluid (water), as depicted in Figure 2. These are characterised by two shear layers separated by a velocity maximum. The lower shear layer is generated by basal drag and is stratified in nature, whereas the upper shear layer is a result of drag with the ambient fluid and is subsequently more mixed. h is the height of the current defined by the Ellison and Turner [1959] method in Table 1, ρ_a and ρ_s are the densities of the ambient and saline fluid respectively, and h_{max} and u_{max} are the height and magnitude of the velocity maximum.

2 Method:

2.1 Laboratory Setup:

A series of continuous release saline gravity current experiments were conducted in the Sorby Environmental

Fluid Dynamics Laboratory at the University of Leeds. While saline currents do not allow for the study of particulate settling, they do provide a good dynamical model of turbulent and stratification effects in turbidity currents [Kneller & Buckee, 2000; Islam & Imran, 2010; Cossu & Wells, 2012]. The flume used measured 1.7 m x 1.7 m and had a water depth of 1.5 m. An additional 1 m long inlet channel, along which the currents developed, was centred on one side wall. The entire flume was inclined at an angle of 2° downstream. A fibreglass channel model was placed on a suspended floor 0.4 m above the tank base, with the area underneath acting as a sump to collect denser than ambient fluid.

The channel model is 0.22 m wide and extended the entire length of the inlet channel and 1.5 m into the main flume. The channel-levee profile was designed specifically to create an environment that might replicate morphology found in the field. The channel itself was 0.0275 m deep, giving an aspect ratio of 8, and the channel profile took the form of a sine curve to give a maximum slope of 22° on the channel sides. Channel size and width/depth ratio were chosen to balance the need for deep enough flows to be fully turbulent, while achieving a low aspect ratio as is often seen in the field [Clark et al., 1992; Kenyon et al., 1995]. The channel is bounded by a 22 cm wide levee on either side. The outer part of the levee profile is determined by the relationship $z = H(L/Y)^{-B}$, where z is the height of the levee, H is the channel depth, L is the distance from the channel thalweg, Y is half the channel width, and $B = 0.5535S^{0.662}$, where S is the slope. This was found to be give the best fit to channel levees on slopes >0.6° by Nakajima and Kneller [2013]. Although this relationship works well for the far field architecture it fails to capture the morphology near the crest. Therefore, the inner third of the levee profile was determined using data from previous gravity current experiments conducted over an erodible bed [Straub et al., 2008].

The gravity currents were created by preparing a saline solution of 1025 kg/m^3 density (2.5% excess density). The solution was pumped into the tank and controlled by an electromagnetic flow meter to minimise variation in the input flow rate. Before entering the tank, the fluid passed through a momentum diffuser, manufactured by capping the input pipe and drilling a series of holes in the pipe wall; this pipe was placed within a further inlet pipe which fed an inlet box modelled to fit the channel profile. This ensured that a buoyancy driven flow developed, rather than a dynamically different wall jet driven by inherited momentum and pressure (see supplementary material). Fluid was also pumped out from the base of the tank at an equal rate to ensure a constant water depth. Three flow rates were investigated: 0.2, 1 and 2 l/s (Table 2). The 0.2 l/s flow rate was chosen to give a near bank-full current. The 1 l/s flow rate was chosen to ensure a large enough quantity of overbank spill to measure with the ADVs (see below). The 2 l/s flow rate was chosen as the largest achievable rate for which an appropriate flow duration could be achieved (4 minutes) without over-filling the sump.

Hereafter these will be referred to respectively as bank-full, equilibrium, and oversize currents (Table 2).

Instantaneous three-component velocities were captured with a profiling Nortek Vectrino II acoustic Doppler velocimeter (ADV) sampling at 100 Hz. Vertical resolution of the data is 1 mm with each profile extending 30 mm above the model base. Velocities were recorded both at the channel thalweg and the channel crest.

Ultrasonic Doppler velocity profiling (UDVP) was used at the channel thalweg to capture larger velocity profiles. The ADV velocity profiles were extended with the UDVP data for the purposes of calculating bulk flow properties.

Input Flow Rate (l/s)	0.2 (bank-full)	1 (equilibrium)	2 (oversize)
h (cm)	3.17	4.75	5.33
U (m/s)	0.111	0.153	0.174
Re	3550	7250	9250
Fr/Ri	1.50/0.44	1.65/0.37	1.77/0.32
Flow duration	8 minutes	4 minutes	4 minutes

Table 2: Bulk flow properties of the three laboratory flows calculated from channel thalweg ADV/UDVP data, 1 m downstream from the main tank inlet.

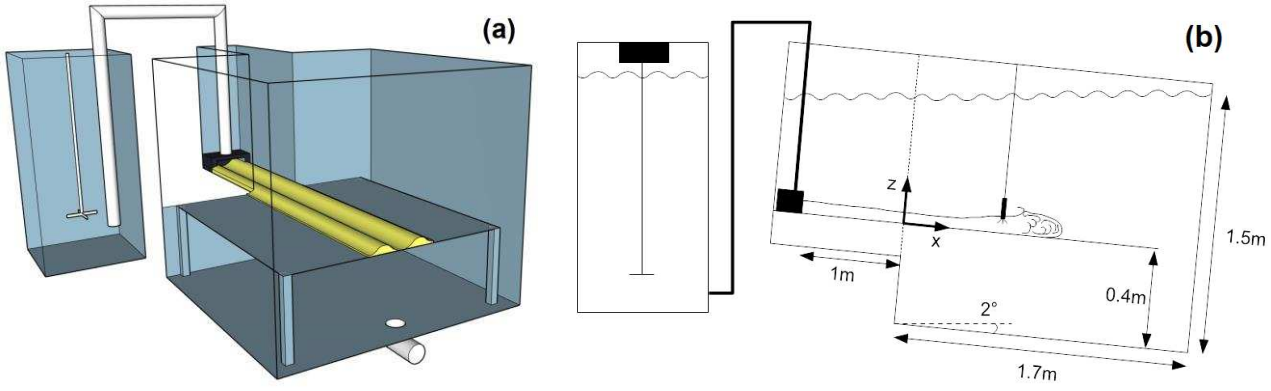

Figure 2: (a) A 3D visualisation (channel profile not to scale) and (b) a cross-sectional schematic of the setup employed in the Sorby Laboratory. Saline was pumped from a large mixing tank via a momentum diffuser into the main tank which was inclined at 2°. A 1 m long confined inlet chan nel allowed the flow to develop. The channel was elevated on a false floor to allow fluid to collect in a sump underneath. The frame of reference is defined relative to the channel, with the origin positioned on the channel thalweg at the entrance to the main tank.

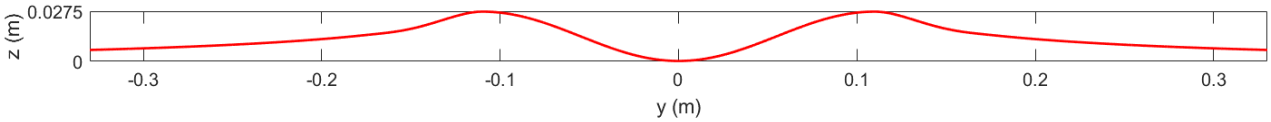

Figure 3: Cross-sectional view of the channel model. The channel measures 0.22 m wide and 0.0275 m deep with an aspect ratio of 8. The profile is that of a sine curve which results in a maximum steepness of 22°. The levee profile was determined using a combination of laboratory data [Straub et al., 2008] and field data [Nakajima and Kneller, 2013].

2.2 Numerical Model:

Numerical simulations of the laboratory flows and additional flow conditions were performed with a Reynolds-averaged Navier-Stokes (RANS) model, solved using the software ANSYS CFX. This is governed by the Reynolds-averaged mass and momentum conservation equations,

$$\frac{\partial \rho}{\partial t} + \nabla \cdot (\rho \boldsymbol{u}) = 0, \tag{2}$$

$$\frac{\partial \rho u_i}{\partial t} + \frac{\partial \rho u_i u_j}{\partial x_j} = -\frac{\partial P}{\partial x_i} + \frac{\partial}{\partial x_j}\left(\mu \frac{\partial u_i}{\partial x_j} - \rho \overline{u_i' u_j'}\right) + \rho f_i, \tag{3}$$

where the velocity terms have been separated into Reynolds-averaged components, u_i, and fluctuating components, u_i'. Reynolds-averaged external forces and pressure are denoted by f_i and P respectively.

A shear stress transport (SST) turbulence closure has been used to model the Reynolds stresses, $-\rho\overline{u_i' u_j'}$. This combines the free-stream capability of the popular k-ϵ model with the explicit wall resolution of the k-ω model, and was found to perform better when compared with the laboratory data. It is still a two-equation eddy viscosity model, with transport equations for k, the turbulent kinetic energy and ω, the turbulence frequency. However, blending functions are utilised in order to exploit the near-wall treatment of the k-ω model and the

free-stream capability of the k-ϵ model [Menter, 1994]. A more detailed description can be found in the supplementary material.

To model variations in flow density, a mixture model was employed. This requires the solving of one conservation of mass equation (2) and one conservation of momentum equation (3) for the mixture. In this case, the mixture comprises water and saline with densities $\rho_w = 1000$ kg/m^3 and $\rho_s = 1025$ kg/m^3, respectively. The density of the mixture is defined by $\frac{1}{\rho} = \frac{1-\alpha}{\rho_w} + \frac{\alpha}{\rho_s}$, where α is the saline mass fraction. This variable density is used in all terms of the model, including that of gravity. Additionally, a transport equation is solved for the saline mass fraction,

$$\frac{\partial \alpha\rho}{\partial t} + \nabla \cdot (\alpha\rho\boldsymbol{u}) = -\nabla \cdot \left(\overline{\alpha'\rho\boldsymbol{u}'}\right), \tag{4}$$

where the Reynolds flux term is modelled using the eddy diffusion hypothesis as,

$$-\overline{\alpha'\rho u_j'} = \frac{\mu_t}{\sigma_t}\frac{\partial \alpha}{\partial x_j}, \tag{5}$$

and μ_t, and $\sigma_t = 1$, are the eddy viscosity and turbulent Schmidt number respectively. Flow conditions and channel morphology were kept identical to laboratory values. Two larger flows with flow rates of 3 and 4 l/s, higher than was possible in the laboratory, were also simulated. Moreover, to investigate the role of Reynolds number, a set of flows were simulated in a channel 4 times larger than in the laboratory. Flow rates were scaled upwards by a factor of 16 to ensure the same flow rate per unit area. Table 3 shows the bulk quantities of these flows.

Use and validation of this modelling approach is extensive both in this field [e.g. Imran et al., 2004, 2007; Giorgio Serchi et al., 2011] and related fields [e.g. Gauer at al., 2005; Doronzo, 2013]. Additionally, the numerical model has been compared to the experimental data in this study (Section 3.1).

Input Flow Rate (l/s)	0.2	1	2	3	4	3.2	16	32	48	64
h (cm)	3.05	4.36	5.01	5.43	5.69	11.7	15.1	17.2	18.5	19.4

U (m/s)	0.111	0.151	0.175	0.194	0.212	0.179	0.294	0.325	0.353	0.377
Re	3390	6580	8770	10500	12100	20900	44300	55900	65100	73300
Fr	1.64	1.84	1.96	2.03	2.15	1.77	1.89	1.89	1.97	2.06
Ri	0.372	0.295	0.260	0.243	0.216	0.321	0.251	0.281	0.257	0.235

Table 3: Bulk flow properties of the numerically simulated flows calculated from channel thalweg data, 1 m downstream from the main tank inlet. Flows in the left column traverse the laboratory scale channel, with the flows in the right column traversing a channel scaled 4 times larger.

3 Results:

3.1 Velocity and density structure:

The velocity profiles of the three laboratory flows are shown in Figure 4. These were captured with an ADV 1 m downstream of the main tank inlet to allow the flows to develop. As has been observed in many previous studies [e.g. Ellison and Turner, 1959; Garcia and Parker, 1993; Islam and Imran, 2010] all profiles exhibit a lower shear layer caused by basal drag and an upper shear layer caused by drag and subsequent mixing with the ambient fluid. These are separated by a velocity maximum. Here, the height of the velocity maximum remains almost constant for all flows at a height equal to half the channel depth. This is despite the changes in flow height, discharge, and Richardson number, suggesting that channel depth is a key control on partially-confined flow development.

The numerical simulations predict velocity profiles that compare well with the laboratory data (Figure 5) and model performance is comparable to previous gravity current studies [e.g. Huang et al., 2005; Giorgio Serchi et al., 2011]. Except for the bank-full flow, the constant velocity maximum height is replicated (Figure 6) and the simulations show it remains constant at flow magnitudes larger than were possible in the laboratory. The upper shear layers are captured well, although the numerical simulations predict slightly different magnitudes for the maximum velocity and lower shear layer. In accordance with previous laboratory [e.g. Sequeiros et al., 2010; Islam and Imran, 2010] and numerical studies [e.g. Imran et al., 2004, 2007; Giorgio Serchi et al., 2011; Kneller et al., 2016], the simulations provide density data that show a stratified region below the velocity

maximum with an increasingly mixed region above. The collapse of the simulated profiles in the lower shear layer (Figure 6) shows the bank-full flow to be characteristically different to the larger, overspilling flows, suggesting that overspill plays an important role in the development of flow structure.

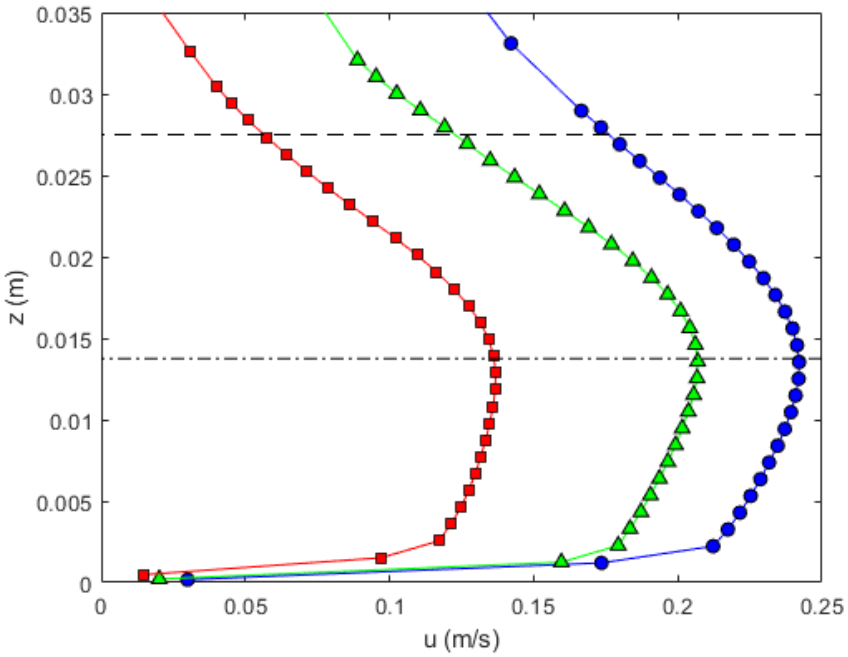

Figure 4: Channel thalweg ADV velocity profiles measured 1 m downstream from the main tank inlet, time-averaged over a 3 minute period. Red squares – 0.2 l/s; Green triangles – 1 l/s; Blue circles – 2 l/s. The dashed lines indicate channel depth and half channel depth. The height of the velocity maximum remains almost constant despite changes in flow rate and depth. This is in contrast to confined flows where velocity maximum height scales with flow depth.

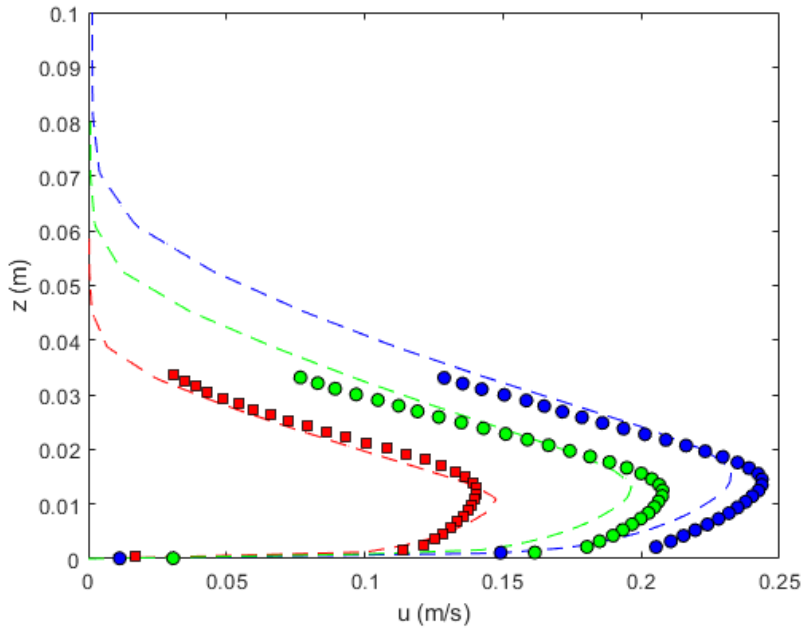

215

216 **Figure 5**: Channel thalweg ADV (symbols) and numerical (dashed lines) velocity profiles, measured 1 m
217 downstream from the main tank inlet and time-averaged over a 3 minute period. Red- 0.2 l/s; Green - 1 l/s;
218 Blue - 2 l/s. Data is not normalised to explicitly show similarities and differences.

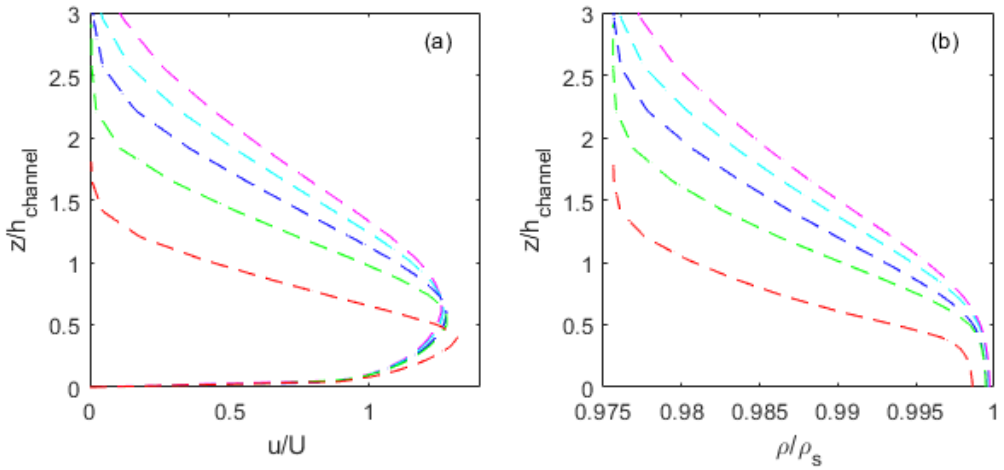

219

220 **Figure 6**: Channel thalweg numerical velocity (a) and density (b) profiles, normalised with depth averaged
221 velocity/saline density and channel depth, measured 1 m downstream from the main tank inlet and time-
222 averaged over a 3 minute period. Red – 0.2 l/s; Green – 1 l/s; Blue 2 l/s; Cyan – 3 l/s; Magenta 4 l/s. Numerical
223 simulations show a constant velocity maximum height for larger flow rates and heights than could be achieved
224 in the laboratory. With the exception of the bank-full flow (red trace), both velocity and density profiles collapse
225 well in the lower shear layer where large levels of stratification are present.

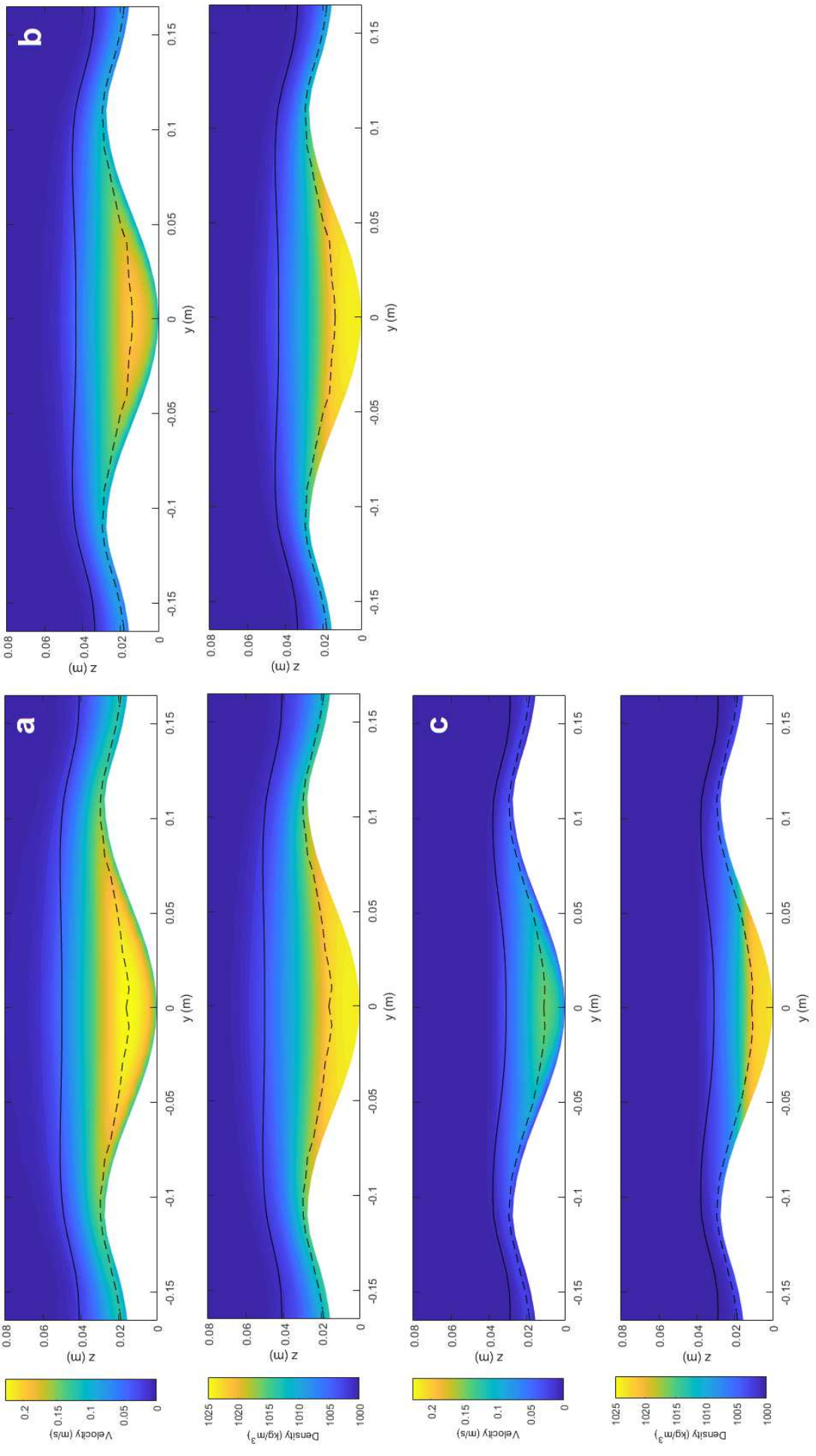
a
b
c
z (m)
y (m)
Velocity (m/s)
Density (kg/m^3)

Figure 7: a) 2 l/s; b) 1 l/s; c) 0.2 l/s. Numerical velocity and density contours. The solid line shows the flow height and the dashed line shows the velocity maximum height. A non-mixed, stratified region below the velocity maximum height is evident in all flows. The channel also appears to maintain a confined 'high-velocity core'.

3.2 High Reynolds number simulations

In order to investigate the effect of Reynolds number, flows were simulated in a channel scaled four times larger than the laboratory geometry. To compare to the laboratory scale flows, flow rates were scaled upwards by a factor of 16 to keep the same flow rates per unit area. The resultant flows had Reynolds numbers between 20,900 and 73,300 (Table 3). The thalweg velocity and density profiles are shown in Figure 8. Similarly to the laboratory scale flows, the height of the velocity maximum of these larger remains fixed at around half the channel depth. The smallest, bank-full flow shows distinctly different characteristics with a relatively faster, more mixed core.

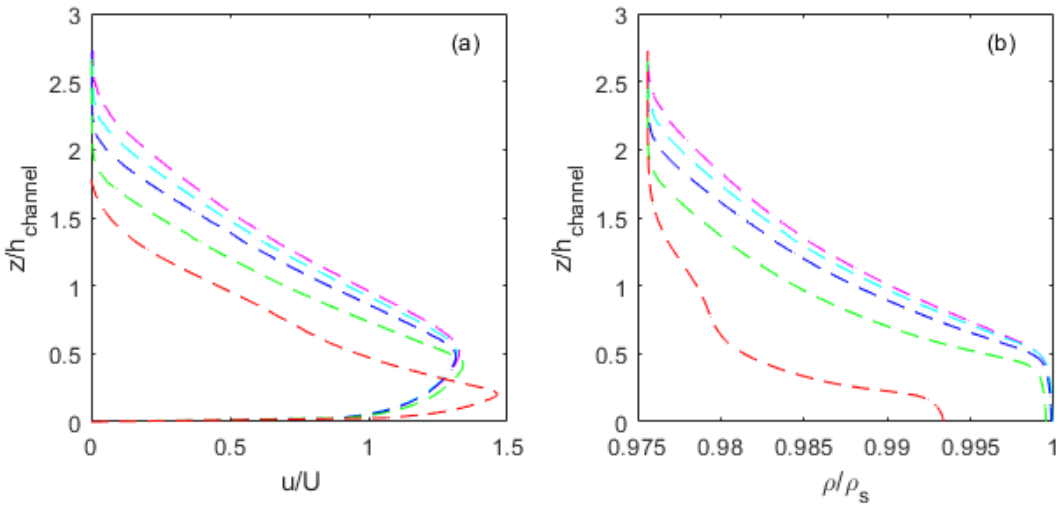

Figure 8: Channel thalweg numerical velocity (left) and density (right) profiles for the higher Reynolds number flows traversing the scaled-up channel. Profiles are normalised with depth averaged velocity/saline density and channel depth, measured 4 m downstream from the main tank inlet. Red – 3.2 l/s; Green – 16 l/s; Blue 32 l/s; Cyan – 48 l/s; Magenta 64 l/s.

3.3 Flow evolution and overspill:

Total streamwise and overbank discharges are shown in Figure 9 using both the laboratory and numerical data. The simulations predict the downstream discharge well, showing close agreement with both the

magnitudes and the spatial evolution. The downstream evolution of the overbank losses is also predicted well, although magnitudes for the two larger flows were over-predicted by 13-73%.

The three currents clearly interact with the channel in different ways. The bank-full current is dominated by ambient entrainment and as a result the streamwise discharge increases downstream. Overbank losses subsequently also increase as the current inflates and overspills the confinement of the channel. Both the streamwise discharge and overbank losses of the equilibrium current remain fairly constant, suggesting a balance between entrainment and overspill. The oversize current exhibits large initial overbank losses which result in a reduction in streamwise discharge. Overspill rates reduce rapidly downstream however as the current size reduces. These are examples of the two main ways - inflation vs. deflation - in which a current can evolve and be 'tuned' to equilibrium by a channel.

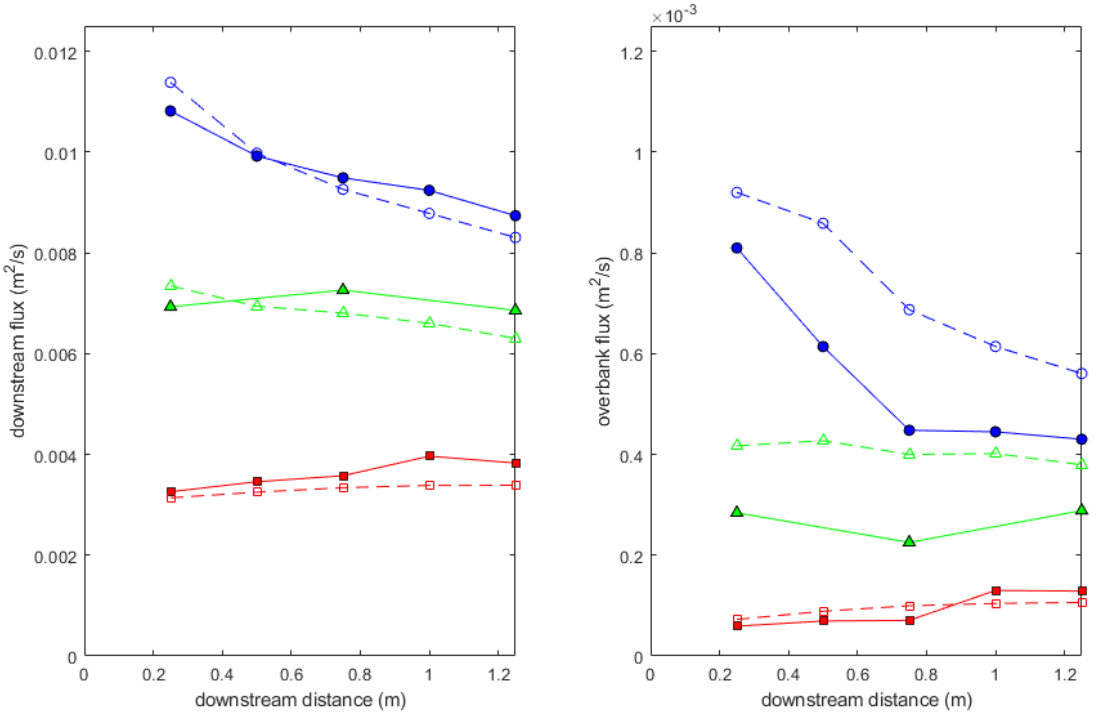

Figure 9: Downstream evolution of streamwise and overbank discharges from laboratory data (solid) and numerical simulations (dashed). Red – 0.2 l/s; Green – 1 l/s; Blue 2 l/s. The simulations predict the spatial evolution well, although they overestimate the magnitude of overspill for the two larger flows. Flow tuning is evident in the different ways each flow evolves. Both the streamwise and overbank discharge of the 0.2 l/s flow increase downstream as ambient fluid is entrained and the flow inflates. The discharges of the 1 l/s flow remain relatively constant indicating a close-to-equilibrium balance between overbank losses and ambient entrainment. The discharge of the 2 l/s flow changes rapidly with large initial overbank losses. The streamwise

discharge continues to reduce downstream, despite ambient entrainment.

3.4 Entrainment:

The entrainment of a flow can be found by a depth integration of the incompressibility equation,

$$\frac{\partial}{\partial x}\int_0^\infty u\,dz + \frac{\partial}{\partial y}\int_0^\infty v\,dz + w_\infty = 0, \tag{6}$$

where $w_\infty = \partial h/\partial t - w_e$ is a product of the shallow-water approximation [Parker, 1986]. Assuming a temporally stable flow, and using definitions in Table 1, this becomes,

$$e_W|U| = \frac{\partial Uh}{\partial x} + \frac{\partial Vh}{\partial y}, \tag{7}$$

where the entrainment velocity, $w_e = e_W|U|$, has been defined as a product of the entrainment coefficient, e_W, and the depth-averaged velocity magnitude of the flow. The entrainment coefficient describes the ability of a flow to entrain ambient fluid. For fully-confined flows with no cross-stream variation, (7) becomes,

$$e_W U = \frac{\partial Uh}{\partial x}, \tag{8}$$

which is the standard form used for confined laboratory flows [Parker, 1987]. For partially-confined flows in a straight channel, when integrated across the channel from thalweg to crest, (5) becomes,

$$\hat{e}_W|\widehat{U}|Y = \frac{\partial \widehat{U}A}{\partial x} + V(Y)h(Y), \tag{9}$$

where the cross-sectional area of the current is defined as $A = \int_0^Y h\ dy$, channel average velocities as $|\widehat{U}| = \left(\int_0^Y \int_0^h |u|\,dz\,dy\right)/A$, the channel average entrainment coefficient as $\hat{e}_W = \left(\int_0^Y e_W\,|U|\,dy\right)/|\widehat{U}|Y$, and Y is half the channel width. The values of e_W presented here are all calculated using (9). If (8) is used for an overspilling, partially-confined flow, negative values will be observed if the current is deflating. Such a current is still clearly entraining ambient fluid and shows how overspill must be taken into account when analysing the entrainment characteristics of such flows. A channel-average Richardson number, defined as the mean of the thalweg and crest Richardson number, is also used in order to account for cross-stream variations.

Both the laboratory and numerical data output entrainment coefficients of the same order of magnitude (Figure 10), with the range of simulated values overlapping with the laboratory counterparts. However the simulated

values, based on the numerical velocity and density data, largely predict higher values. This is attributed mostly to the overprediction over overbank losses (Figure 9). The difference between simulated and laboratory values is largest for the 1 l/s flow which is attributed to the lower longitudinal resolution in the laboratory data for this flow. A clear difference can be seen between the bank-full and the larger, overspilling flows. The dependence of e_W on Richardson number for fully-confined flows, described by Parker et al., [1987] using (1), still appears to hold for the partially-confined setting. Figure 11 shows how the data presented here fall within the scatter of the previous laboratory data. However, there is also an apparent upper bound on e_W for these partially-confined flows. Neither an increase in flow magnitude, nor a reduction in Richardson number, results in a change in e_W (Figures 10 and 11), perhaps suggesting a limit imposed on the entrainment ability of a current by the channel.

Further evidence for the 'tuning' effect of the channel described above is displayed in Figure 12. The downstream evolution of the Richardson number shows how each flow approaches an equilibrium. This is particularly evident in the thalweg. Cross-sectional contours of gradient Richardson number in Figure 13, produced using numerical simulation data, show how the stability of the stratification varies throughout each of the flows. The vertical structure is typical of a gravity current [Kneller et al., 2016], with values approaching infinity around the velocity maximum due to the reversal of the velocity gradient while a less stable layer above this that helps to drive entrainment. Here, localised low gradient Richardson regions are seen over the levee crests.

A reduction in bulk Richardson number is also seen over the levee crests for all flows. Similar cross-stream variations and magnitudes are found for the gradient Richardson number when depth-averaged over the upper shear layer. The depth-averaging region was defined to be between 0.5 and 2.5 standard deviations above the velocity maximum, found by approximating the upper velocity profile with a Gaussian distribution. This region was chosen to include the entire upper shear layer which is responsible for ambient entrainment while excluding the very high magnitudes found around the velocity maximum. This region also spans above the flow height determined by the Ellison and Turner [1959] definition (Table 1) which is used in the calculation of bulk quantities.

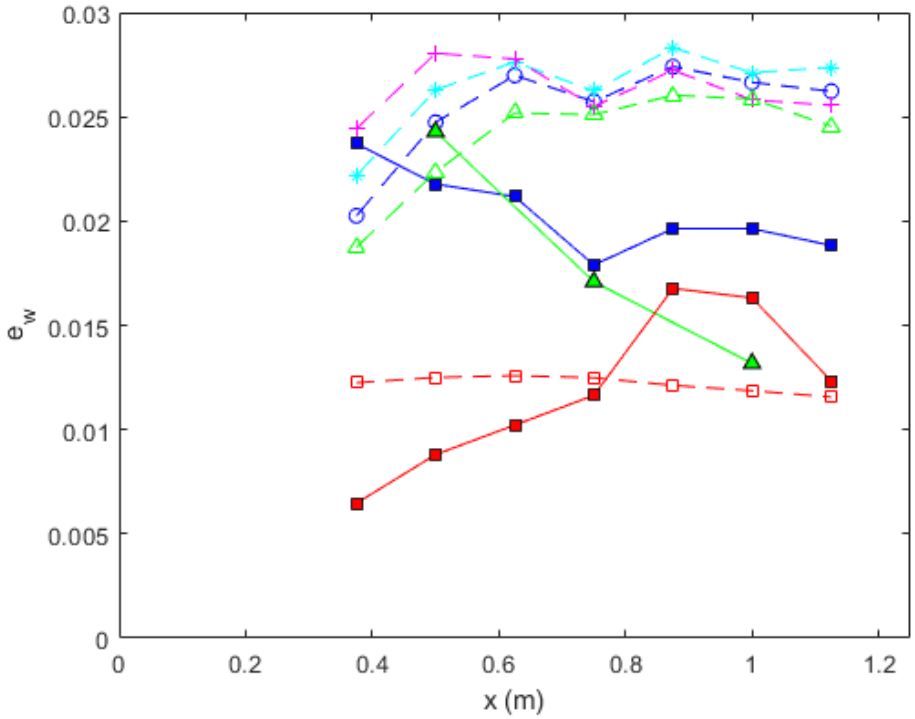

Figure 10. Downstream evolution of entrainment coefficient. Laboratory – solid; Numerical – dashed. Red – 0.2 l/s; Green – 1 l/s; Blue 2 l/s; Cyan – 3 l/s; Magenta 4 l/s. The magnitudes of the entrainment coefficient show overlap between the numerical and experimental data, although the simulations largely predict slightly higher values.

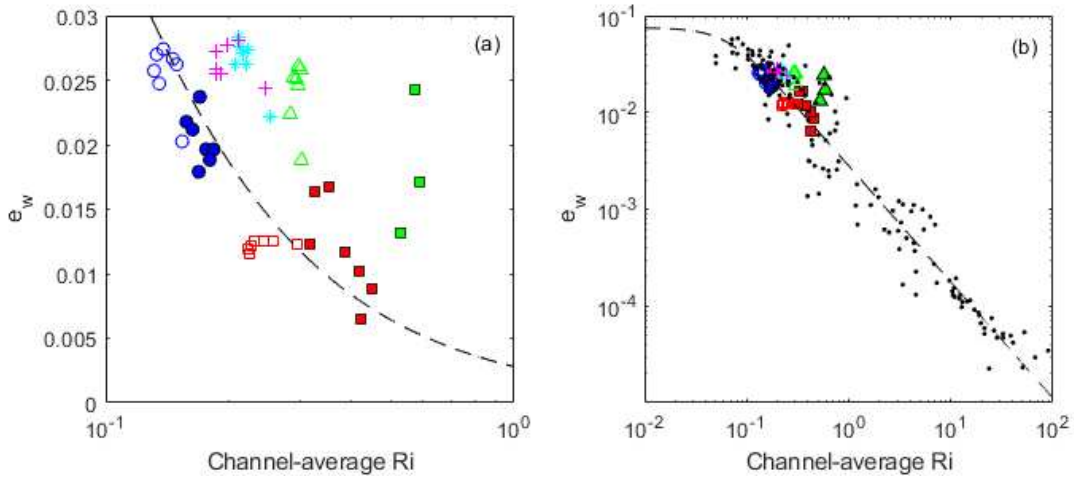

Figure 11. Entrainment coefficient is dependent on the (channel-average) Richardson number. Laboratory – filled; Numerical – hollow. Red – 0.2 l/s; Green – 1 l/s; Blue 2 l/s; Cyan – 3 l/s; Magenta 4 l/s. Data shown on a linear (a) and logarithmic (b) axis. The dashed line indicates the Parker et al. [1987] relationship (1). Previous experimental data from confined flows, collated by Parker et al., are shown in black on the right [Ellison and Turner, 1959; Lofquist, 1960; Ashida and Egashira, 1975]. The standard deviation of the entrainment

coefficient from the defined relationship is 0.041 for the previous confined data and 0.015 for the data presented here.

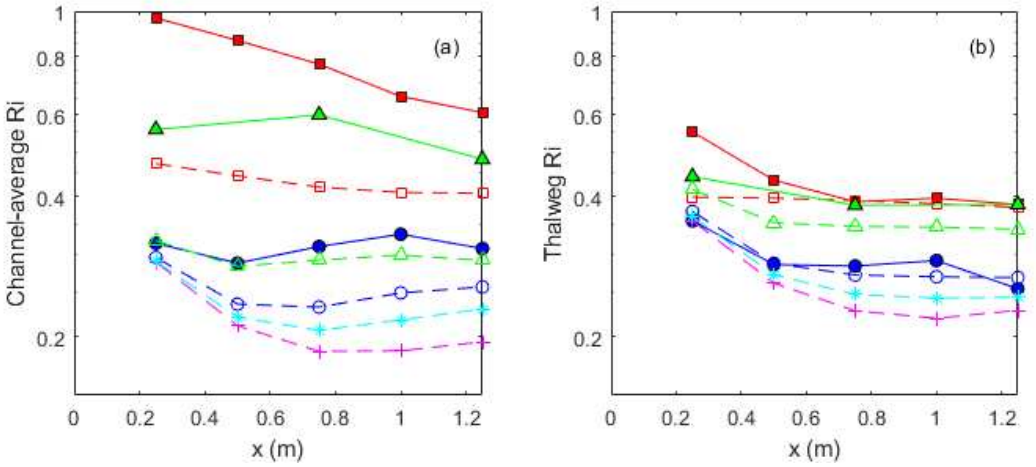

Figure 12. Downstream development of channel-average (a) and thalweg (b) Richardson number. Laboratory – solid; CFD – dashed. Red – 0.2 l/s; Green – 1 l/s; Blue 2 l/s; Cyan – 3 l/s; Magenta 4 l/s. CFD density data are used in the calculation of the laboratory values in the absence of laboratory density data. There is an adjustment period before each flow approaches an equilibrium Richardson number, the distance of which is dependent on flow magnitude.

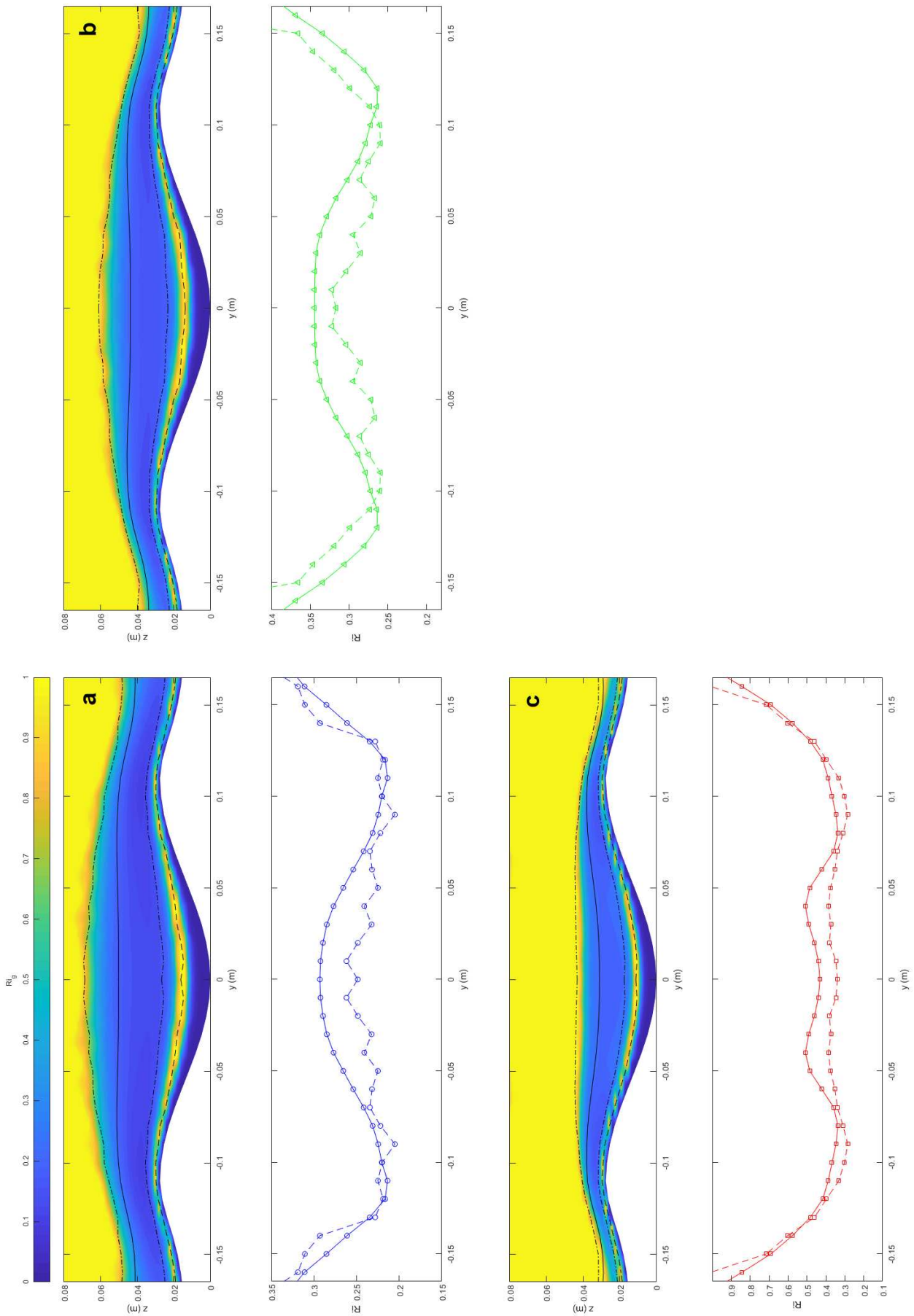

Figure 13: a) 2 l/s; b) 1 l/s; c) 0.2 l/s. Gradient Richardson contours for each flow rate exhibit regions of

decreased magnitudes above the levee crests, and indication of decreased stability and increased mixing. Both the cross-stream variations and magnitudes of the bulk Richardson number (solid line) are comparable with the depth-averaged gradient Richardson number (dashed line). The bulk Richardson number would appear to be a good proxy for the gradient Richardson number in the upper shear layer and a good indication of mixing levels. The depth-average was calculated between 0.5 and 2.5 standard deviations (dash-dot lines) above the velocity maximum (dashed line). The flow height is also shown with a solid line.

4 Discussion:

4.1 Channel forcing

The occurrence of overspill and associated inherent cross-stream variation mean the dynamics of a partially-confined flow are fundamentally different to those of a fully-confined flow. For a fully-confined flow, the velocity maximum height, h_{max}, is determined solely by the balance between basal and ambient drag [Middleton, 1993]; h_{max} scales with height, with values observed between $h_{max}/h = 0.1$ [Buckee et al., 2001] and $h_{max}/h = 0.3$ [Kneller et al., 1999]. Variations are to be expected with differences in basal materials, laboratory conditions and the difficulty in defining a current's height. A dependence of h_{max} on both the flow's Richardson number [Sequeiros et al., 2010] and Reynolds number [Stagnaro and Pittaluga, 2014] has also been observed. For the partially-confined flows analysed here, h_{max} remains nearly constant for all the laboratory-scale flows at a height equal to half the channel depth, regardless of flow height or Richardson number. This could suggest an increase in the ratio of ambient to basal drag for larger flows, perhaps due to the increase in overspill and the surface area of the ambient interface. For the upscaled flows, described in Section 3.2, the smaller flows have a relatively lower position of h_{max}. This can be explained by the basal drag remaining constant but ambient drag increasing with Reynolds number. However, half the channel depth remains as an upper limit on h_{max} for the larger flows indicating that, even at large Reynolds numbers, channel depth remains a first-order control on flow structure.

It would appear the channel has the ability to maintain a high velocity 'core' (illustrated in Figure 7). A value of h_{max} less than the channel depth allows the current to maintain a highly stratified lower region confined by the base of the channel. This region provides a gravitational driving force that is sustained along the length of the channel and enables the possibility of a stable downstream flow evolution pattern. The forcing on the current exerted by the channel is therefore further confirmed as a key control on the flow dynamics and can be recognised as an important mechanism in sustaining current run-out.

363 It is unclear at what point h_{max} could exceed the channel depth, although this would make a rapid dissipation
364 of the current likely, with the lower region no longer fully restricted and nothing to prevent lateral spreading. In
365 a laboratory study with varying levels of flow confinement, Mohrig and Buttles [2007] defined a threshold of
366 $h/H > 5$, where H is the channel depth to differentiate confined vs. effectively unconfined flow. It was proposed
367 that at this threshold the high velocity core exceeds the confines of the channel, resulting in an unconfined
368 flow, although there was no vertical resolution in the velocity data which were acquired from overhead
369 cameras. The laboratory and simulated flows described here have values in h/H ranging from 1.15 to 3. While
370 none of these flows approach the $h/H > 5$ threshold, the constant height of the velocity maximum suggests
371 any transition would not be gradual.

372 **4.2 Numerical model performance**

373 A numerical RANS model with a shear stress transport turbulence closure has been used to simulate flows
374 with magnitudes too large to produce in this laboratory setup and investigate the role of higher Reynolds
375 numbers. Performance, in terms of agreement with laboratory velocity data, is comparable to those of similar
376 models [e.g. Imran et al., 2007; Giorgio Serchi et al., 2011]. Crucially, the numerical model helps to show how
377 the constraint of the half channel depth on the velocity maximum height is not an artefact of the lower Reynolds
378 numbers found in the laboratory. An increase in Reynolds number (Section 3.2), and the resultant increase in
379 ambient drag, has limited impact on this upper constraint. The comparison between the laboratory and
380 numerical velocity profiles (Figure 5) shows reasonably good agreement, particularly with the velocity gradients
381 in the shear layers. However, there are still clear differences between the simulations and the experiments.
382 While the velocity maximum heights are predicted well for the 1 and 2 l/s flows, the height is underpredicted
383 for the smallest 0.2 l/s flow. There are also discrepancies of up to 7% in the magnitudes of the velocity maxima.
384 The modelling of the stratification and subsequent levels of overbank losses could be one source of these
385 errors, with Figure 9 showing significant overprediction of overbank loss. Furthermore, the time-averaging
386 introduced in RANS modelling could not completely capture the effect of large-scale, transient flow features
387 such as the mixing introduced by Kelvin-Helmholtz instabilities at the ambient interface. Finally, the use of
388 numerical density data in the calculation of laboratory Froude number and entrainment coefficient values
389 means that discrepancies in these areas are introduced solely from the observed differences in velocity data.

390 **4.3 Flow tuning**

391 A channel is clearly capable of 'tuning' oversize flows via overspill, with deflation and flow stripping occurring
392 here for flows with $h/H > 1.9$. Mohrig and Buttles [2007] also observed this tuning effect, reporting flows with

$h/H > 1.3$ undergoing deflation until a constant flow height was reached. At the laboratory scale at least, such oversize flows appear to be unable to propagate in a partially-confined setting. While it is therefore unlikely the $h/H > 5$ threshold would be breached via gradual flow evolution, external factors could trigger this scenario. A current emerging from a canyon system could be disproportionally deep before being stripped or thinned by the channel, analogous to the oversize current described here that experienced significant overspill proximally (Figure 9). A break in slope, as often seen at a channel-lobe transition zone [Wynn et al., 2002; Dorrell et al., 2016], could also cause a sudden thickening of the flow and a subsequent avulsion or transition to unconfinement. Additionally, increasing channel instability, caused by continual deposition, could lead to a channel being unable to provide the necessary degree of confinement to contain the high velocity core [Dorrell et al., 2015]. Here we are considering the dynamics of straight channel confinement; channel sinuosity leads to flow elevation at bend apexes [Keevil et al., 2006; Cossu and Wells, 2010; Dorrell et al., 2013], providing an additional mechanism for flow avulsion.

While the size of the flow can be tuned via overspill, ambient entrainment can also lead to the inflation of an undersize flow. This mechanism allows the achievement of an equilibrium whereby a current's overbank losses are balanced with ambient entrainment. In contrast, entrainment is the sole mechanism for fully-confined flow evolution, resulting in continued inflation [Symons et al., 2017]. Here, a quasi-equilibrium current, characterised by $h/H = 1.75$, can be identified in the 1 l/s case. Both streamwise and overbank discharges remain relatively constant along the length of the channel (Figure 9). Further evidence of tuning can be seen in Figure 12. Each flow must propagate for a characteristic length before attaining a constant Richardson number, with the magnitude of this length correlated with the size of the flow. It is unlikely, however, that for a given channel geometry, there exists a unique equilibrium flow condition that all currents evolve towards regardless of input. Rather, a partially-confining channel allows a range of currents to develop a balance between ambient entrainment and overbank losses which allows stable downstream evolution. These mechanisms are illustrated in Figure 14.

If a channel has the capability to modify flows along its length, an impact in the overbank deposit record would be expected. Differing levels of overspill near the channel inlet followed by an approach to an equilibrium value would suggest a transformation from heterogeneous overbank deposits proximally to homogenous deposits distally. This is, however, based on the assumption that all overbank flow is of a similar depositional character. Larger overbank flows may bypass the channel-proximal levee, significantly complicating the depositional record in these locations.

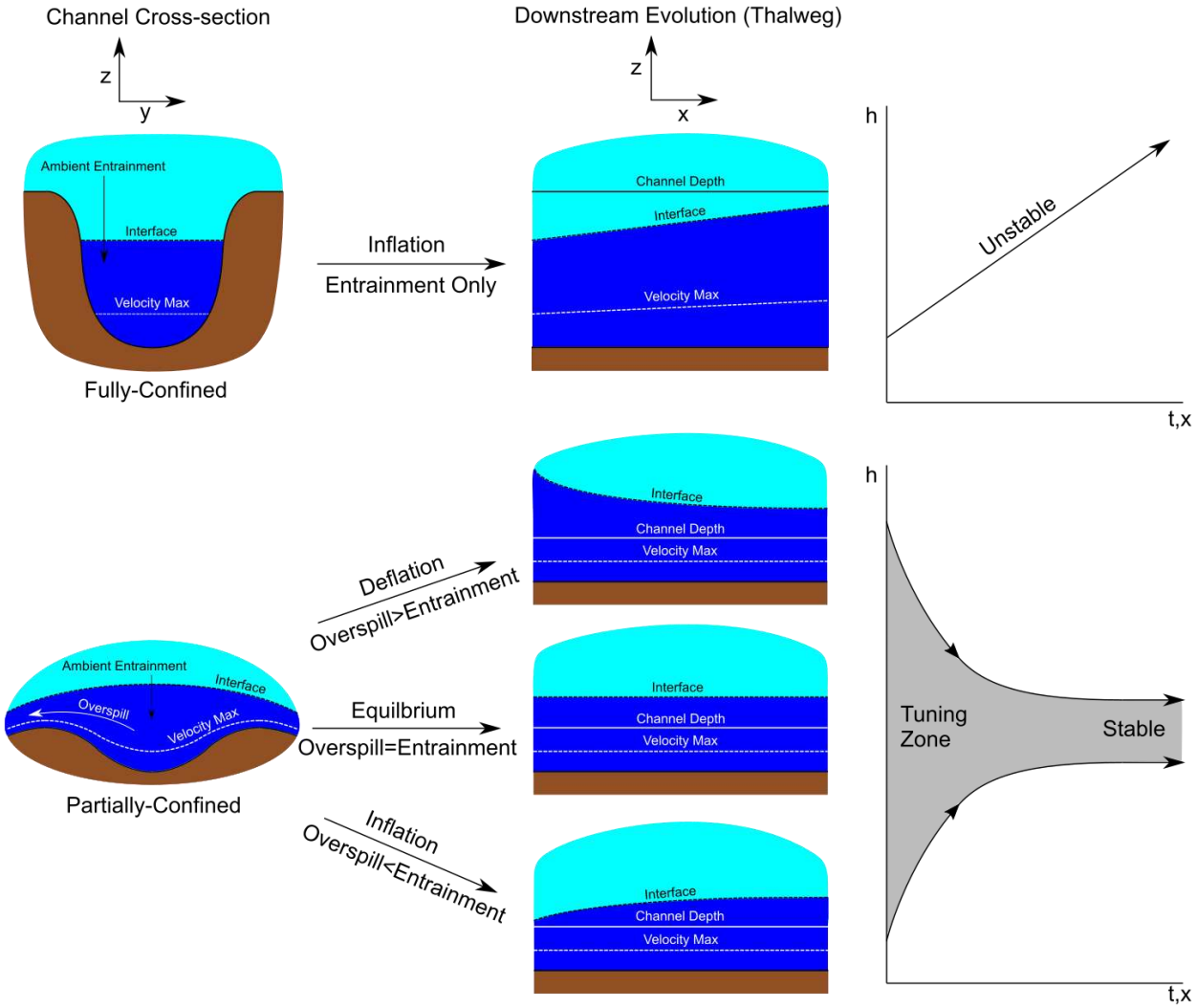

Figure 14: Downstream evolution patterns of fully and partially-confined flows. Entraining fully-confined flows can only inflate in an unstable evolution pattern. Partially-confined flows can either inflate or deflate to approach a stable equilibrium where overbank losses are balanced by ambient entrainment.

4.4 Entrainment and cross-stream variation

It can be seen from (9) that for a partially-confined flow the overspill term, Vh, has a significant impact on the entrainment. This is evident in the markedly lower entrainment coefficient values for the bank-full flow (Figure 10). It is also the primary reason for the difference in simulated and laboratory values (Figure 9 shows how the numerical model over-predicts overspill levels for the larger flows). It is therefore slightly surprising that, for a given Richardson number, these partially-confined flows exhibit similar entrainment rates to fully-confined flows (Figure 11), despite the differences in flow dynamics described above, such as the occurrence of overspill. It should be noted that the calculation of the Richardson numbers for the laboratory flows is dependent on the numerical density data. Given the relatively low spread of this and previous data, however (see Figure 11), it

436 is unlikely any discrepancies would significantly affect the Richardson number calculations or any conclusions
437 drawn.

438 As is the case with the velocity maximum height, there does appear to be an upper limit on flow entrainment
439 efficiency. Despite an increase in input flow rate and a reduction in thalweg Richardson number (Table 3), the
440 larger 3 and 4 l/s laboratory scale flows do not exhibit higher values of entrainment coefficient. This appears
441 to be driven by a lower Richardson number at levee crests resulting in a lower channel average Richardson
442 number and the corresponding associated average entrainment characteristics. Again, the constraints of the
443 channel morphology and the increasing levels of overspill appear to be a key control on flow dynamics.

444 For all the flows considered it is important to take into account cross-stream variations, as these can be
445 significant, affecting not only calculated entrainment levels but also definitions of Richardson number. The bulk
446 Richardson number is often used as an approximation for the gradient Richardson number (see definitions in
447 Table 1), which can be used to identify regions of increased mixing due to buoyant instability. For partially-
448 confined flows, these regions occur above both levee crests (Figure 13) highlighting how mixing processes at
449 channel boundaries are key to the entrainment process. Using 2D direct numerical simulation of the Navier-
450 Stokes equations, Kneller et al. [2016] found that the bulk Richardson number was not a good measure of the
451 gradient Richardson number, which served as a good indicator to a flow's entrainment behaviour. Here though,
452 the bulk Richardson number, for all flows, appears to be a good proxy for the gradient Richardson number in
453 the upper shear layer (Figure 13). This is the region responsible for ambient entrainment and thus of most
454 interest when examining mixing rates. Both the magnitudes and the cross-stream variations are captured well
455 in the numerical modelling reported here. It is possible that the 2D nature of the simulations reported by Kneller
456 et al. [2016] may have resulted in the artificial dampening of some of the flow's mixing mechanisms.

457 **5 Conclusions:**

458 Both laboratory experiments and numerical simulations show that for a partially-confined gravity current the
459 geometry of the containing channel is a first-order control on the flow dynamics. Here, at the laboratory scale,
460 the height of the velocity maximum for a range of flows was not affected by changes in multiple factors including
461 flow height and Richardson number. The velocity maximum remained fixed at a height equal to half the channel
462 depth, which resulted in the development of a high-velocity core and highly stratified lower shear layer, both
463 confined within the channel. Numerical simulations at larger Reynolds numbers confirm the half channel depth
464 upper limit on the velocity maximum height. The channel form plays a key factor in controlling the downstream
465 evolution of the current. The joint mechanisms of overspill and ambient entrainment allow partially-confined

flows to either deflate or inflate towards a quasi-equilibrium state. There are significant cross-stream variations in the Richardson and gradient Richardson numbers of partially-confined flow. Low Richardson number regions observed over the levee crests indicate increased levels of mixing and highlight the importance of overspill in the entrainment process. Despite this, the entrainment coefficients for a given Richardson number are similar to those of fully-confined flows in previous studies.

Acknowledgements:

This work is supported by the Engineering and Physical Sciences Research Council (EPSRC) Centre for Doctoral Training in Fluid Dynamics grant EP/L01615X/1 and the TRG consortium (Anadarko, BG-Group, BHP-Billiton, BP, Conoco Phillips, Equinor, Marathon Oil, Maersk Oil, Nexen, Tullow, and Woodside). We thank Kyle Straub for providing laboratory data used in the channel design process and Helena Brown, Gareth Keevil and Robert Thomas for their invaluable help in the Sorby Laboratory. We also thank two anonymous reviewers whose valuable input led to an improvement in this work, Laboratory ADV data and ANSYS input and output files can be found at https://doi.org/10.5518/412.

References:

Abd El-Gawad, S., Cantelli, A., Pirmez, C., Minisini, D., Sylvester, Z. and Imran, J., 2012. Three-dimensional numerical simulation of turbidity currents in a submarine channel on the seafloor of the Niger Delta slope. Journal of Geophysical Research: Oceans, 117(C5).

Ashida, K. and Egashira, S., 1975, May. Basic study on turbidity currents. Proceedings of the Japan Society of Civil Engineers, 237, pp. 37-50.

Azpiroz-Zabala, M., Cartigny, M.J., Sumner, E.J., Clare, M.A., Talling, P.J., Parsons, D.R. and Cooper, C., 2017. A general model for the helical structure of geophysical flows in channel bends. Geophysical research letters, 44(23).

Bonnecaze, R.T., Huppert, H.E. and Lister, J.R., 1993. Particle-driven gravity currents. Journal of Fluid Mechanics, 250, pp.339-369.

Buckee, C., Kneller, B. and Peakall, J., 2001. Turbulence structure in steady, solute-driven gravity currents. Particulate Gravity Currents, IAS Spec. Publ., 31, pp.173–187.

Cantero, M.I., Balachandar, S., Cantelli, A., Pirmez, C. and Parker, G., 2009. Turbidity current with a roof:

493 Direct numerical simulation of self-stratified turbulent channel flow driven by suspended sediment. Journal of
494 Geophysical Research: Oceans, 114(C3).

495 Clark, J.D., Kenyon, N.H. and Pickering, K.T., 1992. Quantitative analysis of the geometry of submarine
496 channels: implications for the classification of submarine fans. Geology, 20(7), pp.633-636.

497 Cossu, R. and Wells, M.G., 2010. Coriolis forces influence the secondary circulation of gravity currents flowing
498 in large-scale sinuous submarine channel systems. Geophysical Research Letters, 37(17).

499 Cossu, R. and Wells, M.G., 2012. A comparison of the shear stress distribution in the bottom boundary layer
500 of experimental density and turbidity currents. European Journal of Mechanics-B/Fluids, 32, pp.70-79.

501 Curray, J.R., Emmel, F.J. and Moore, D.G., 2002. The Bengal Fan: morphology, geometry, stratigraphy, history
502 and processes. Marine and Petroleum Geology, 19(10), pp.1191-1223.

503 De Leeuw, J., Eggenhuisen, J.T. and Cartigny, M.J., 2016. Morphodynamics of submarine channel inception
504 revealed by new experimental approach. Nature communications, 7.

505 Doronzo, D.M., 2013. Aeromechanic analysis of pyroclastic density currents past a building. Bulletin of
506 volcanology, 75(1), p.684.

507 Dorrell, R.M., Darby, S.E., Peakall, J., Sumner, E.J., Parsons, D.R. and Wynn, R.B., 2013. Superelevation and
508 overspill control secondary flow dynamics in submarine channels. Journal of Geophysical Research:
509 Oceans, 118(8), pp.3895-3915.

510 Dorrell, R.M., Darby, S.E., Peakall, J., Sumner, E.J., Parsons, D.R. and Wynn, R.B., 2014. The critical role of
511 stratification in submarine channels: Implications for channelization and long runout of flows. Journal of
512 Geophysical Research: Oceans, 119(4), pp.2620-2641.

513 Dorrell, R.M., Burns, A.D. and McCaffrey, W.D., 2015. The inherent instability of leveed seafloor
514 channels. Geophysical Research Letters, 42(10), pp.4023-4031.

515 Dorrell, R.M., Peakall, J., Sumner, E.J., Parsons, D.R., Darby, S.E., Wynn, R.B., Özsoy, E. and Tezcan, D.,
516 2016. Flow dynamics and mixing processes in hydraulic jump arrays: Implications for channel-lobe transition
517 zones. Marine Geology, 381, pp.181-193.

518 Eidsvik, K.J. and Brørs, B., 1989. Self-accelerated turbidity current prediction based upon (k-ε)
519 turbulence. Continental Shelf Research, 9(7), pp.617-627.

520 Ellison, T.H. and Turner, J.S., 1959. Turbulent entrainment in stratified flows. Journal of Fluid Mechanics, 6(3),
521 pp.423-448.

522 Garcia, M. and Parker, G., 1993. Experiments on the entrainment of sediment into suspension by a dense
523 bottom current. Journal of Geophysical Research: Oceans, 98(C3), pp.4793-4807.

524 Gauer, P., Kvalstad, T.J., Forsberg, C.F., Bryn, P. and Berg, K., 2005. The last phase of the Storegga Slide:
525 simulation of retrogressive slide dynamics and comparison with slide-scar morphology. In Ormen Lange–an
526 Integrated Study for Safe Field Development in the Storegga Submarine Area (pp. 171-178).

527 Giorgio Serchi, F., Peakall, J., Ingham, D.B. and Burns, A.D., 2011. A unifying computational fluid dynamics
528 investigation on the river-like to river-reversed secondary circulation in submarine channel bends. Journal of
529 Geophysical Research: Oceans, 116(C6).

530 Huang, H., Imran, J. and Pirmez, C., 2005. Numerical model of turbidity currents with a deforming bottom
531 boundary. Journal of Hydraulic Engineering, 131(4), pp.283-293.

532 Keevil, G.M., Peakall, J., Best, J.L. and Amos, K.J., 2006. Flow structure in sinuous submarine channels:
533 velocity and turbulence structure of an experimental submarine channel. Marine Geology, 229(3), pp.241-257.

534 Kenyon, N.H., Amir, A. and Cramp, A., 1995. Geometry of the younger sediment bodies of the Indus Fan.
535 In Atlas of Deep Water Environments (pp. 89-93). Springer Netherlands.

536 Khripounoff, A., Vangriesheim, A., Babonneau, N., Crassous, P., Dennielou, B. and Savoye, B., 2003. Direct
537 observation of intense turbidity current activity in the Zaire submarine valley at 4000 m water depth. Marine
538 Geology, 194(3), pp.151-158.

539 Klaucke, Ingo, Reinhard Hesse, and William BF Ryan. "Morphology and structure of a distal submarine trunk
540 channel: the Northwest Atlantic Mid-Ocean Channel between lat 53 N and 44 30′ N." Geological Society of
541 America Bulletin 110.1 (1998): 22-34.

542 Kneller, B.C., Bennett, S.J. and McCaffrey, W.D., 1999. Velocity structure, turbulence and fluid stresses in
543 experimental gravity currents. Journal of Geophysical Research: Oceans, 104(C3), pp.5381-5391.

544 Kneller, B. and Buckee, C., 2000. The structure and fluid mechanics of turbidity currents: a review of some
545 recent studies and their geological implications. Sedimentology, 47(s1), pp.62-94.

546 Kneller, B., Nasr-Azadani, M.M., Radhakrishnan, S. and Meiburg, E., 2016. Long-range sediment transport in
547 the world's oceans by stably stratified turbidity currents. Journal of Geophysical Research: Oceans.

548 Imran, J., Kassem, A. and Khan, S.M., 2004. Three-dimensional modeling of density current. I. Flow in straight
549 confined and unconfined channels. Journal of Hydraulic Research, 42(6), pp.578-590.

550 Imran, J., Islam, M.A., Huang, H., Kassem, A., Dickerson, J., Pirmez, C. and Parker, G., 2007. Helical flow
551 couplets in submarine gravity underflows. Geology, 35(7), pp.659-662.

552 Imran, J., Khan, S.M., Pirmez, C. and Parker, G., 2016. Froude scaling limitations in modeling of turbidity
553 currents. Environmental Fluid Mechanics, 1(17), pp.159-186.

554 Islam, M.A. and Imran, J., 2010. Vertical structure of continuous release saline and turbidity currents. Journal
555 of Geophysical Research: Oceans, 115(C8).

556 Lofquist, K., 1960. Flow and stress near an interface between stratified liquids. The Physics of Fluids, 3(2),
557 pp.158-175.

558 Meiburg, E. and Kneller, B., 2010. Turbidity currents and their deposits. Annual Review of Fluid Mechanics, 42,
559 pp.135-156.

560 Menter, F.R., 1994. Two-equation eddy-viscosity turbulence models for engineering applications. AIAA
561 journal, 32(8), pp.1598-1605.

562 Middleton, G.V., 1966. Experiments on density and turbidity currents: I. Motion of the head. Canadian Journal
563 of Earth Sciences, 3(4), pp.523-546.

564 Middleton, G.V., 1993. Sediment deposition from turbidity currents. Annual Review of Earth and Planetary
565 Sciences, 21(1), pp.89-114.

566 Mohrig, D. and Buttles, J., 2007. Deep turbidity currents in shallow channels. Geology, 35(2), pp.155-158.

Normark, W.R. and Damuth, J.E., 1997. Sedimentary facies and associated depositional elements of the Amazon Fan. In Proceedings of the Ocean Drilling Program. Scientific Results (Vol. 155, pp. 611-651). Ocean Drilling Program.

Parker, G., Fukushima, Y. and Pantin, H.M., 1986. Self-accelerating turbidity currents. Journal of Fluid Mechanics, 171, pp.145-181.

Parker, G., Garcia, M., Fukushima, Y. and Yu, W., 1987. Experiments on turbidity currents over an erodible bed. Journal of Hydraulic Research, 25(1), pp.123-147.

Peakall, J. and Sumner, E.J., 2015. Submarine channel flow processes and deposits: A process-product perspective. Geomorphology, 244, pp.95-120.

Sequeiros, O.E., Spinewine, B., Beaubouef, R.T., Sun, T., García, M.H. and Parker, G., 2010. Characteristics of velocity and excess density profiles of saline underflows and turbidity currents flowing over a mobile bed. Journal of Hydraulic Engineering, 136(7), pp.412-433.

Sequeiros, O.E., 2012. Estimating turbidity current conditions from channel morphology: A Froude number approach. Journal of Geophysical Research: Oceans, 117(C4).

Stagnaro, M. and Pittaluga, M.B., 2014. Velocity and concentration profiles of saline and turbidity currents flowing in a straight channel under quasi-uniform conditions. Earth Surface Dynamics, 2(1), p.167.

Straub, K.M., Mohrig, D., McElroy, B., Buttles, J. and Pirmez, C., 2008. Interactions between turbidity currents and topography in aggrading sinuous submarine channels: A laboratory study. Geological Society of America Bulletin, 120(3-4), pp.368-385.

Sumner, E.J., Peakall, J., Parsons, D.R., Wynn, R.B., Darby, S.E., Dorrell, R.M., McPhail, S.D., Perrett, J., Webb, A. and White, D., 2013. First direct measurements of hydraulic jumps in an active submarine density current. Geophysical Research Letters, 40(22), pp.5904-5908.

Sumner, E.J. and Paull, C.K., 2014. Swept away by a turbidity current in Mendocino submarine canyon, California. Geophysical Research Letters, 41(21), pp.7611-7618.

591 Symons, W.O., Sumner, E.J., Paull, C.K., Cartigny, M.J., Xu, J.P., Maier, K.L., Lorenson, T.D. and Talling,
592 P.J., 2017. A new model for turbidity current behavior based on integration of flow monitoring and precision
593 coring in a submarine canyon. Geology, 45(4), pp.367-370.

594 Talling, P.J., Amy, L.A. and Wynn, R.B., 2007. New insight into the evolution of large-volume turbidity currents:
595 comparison of turbidite shape and previous modelling results. Sedimentology, 54(4), pp.737-769.

596 Talling, P.J., Paull, C.K. and Piper, D.J., 2013. How are subaqueous sediment density flows triggered, what is
597 their internal structure and how does it evolve? Direct observations from monitoring of active flows. Earth-
598 Science Reviews, 125, pp.244-287.

599 Xu, J.P., 2010. Normalized velocity profiles of field-measured turbidity currents. Geology, 38(6), pp.563-566.